Anomalous weathering trends indicate accelerated erosion of tropical basaltic landscapes during the Permo-Triassic warming

Jianghai Yang [a,*], Peter A. Cawood [b], Dan J. Condon [c], Jianzhong Liu [d], Xusheng Deng [d], Jingfu Wang [e], Yuansheng Du [a], Dongxun Yuan [f]

[a] *State Key Laboratory of Biogeology and Environmental Geology, School of Earth Sciences, China University of Geosciences, Wuhan, 430074, China*
[b] *School of Earth, Atmosphere & Environment, Monash University, Melbourne, VIC 3800, Australia*
[c] *NERC Isotope Geosciences Laboratory, British Geological Survey, Keyworth NG12 5GG, UK*
[d] *Bureau of Geology and Mineral Exploration and Development Guizhou Province, Guiyang, 550000, China*
[e] *Institute of Geochemistry, Chinese Academy of Sciences, Guiyang 550002, China*
[f] *School of Resources and Geosciences, China University of Mining and Technology, Xuzhou 221116, China*

ABSTRACT

Weathering of basalt in tropical environments is sensitive to climate change and considered to play a significant role in regulating climate evolution. Though extensively studied on the modern Earth and hypothesized for the geological past, basalt weathering is difficult to directly track in geological archives. We here focus on the basaltic sediments derived from the Emeishan large igneous province (LIP) in South China and determined their organic carbon content and isotope, mineral and geochemical compositions. Based on the newly obtained high-precision zircon U-Pb age of $251.79 \pm 0.12/0.13/0.36$ Ma, we establish temporal variations of weathering intensity for the Emeishan LIP basaltic landscapes in the tropical latitudes through the Permo-Triassic rapid climate warming periods. Analysis of weathering trends indicates a significant decrease in weathering intensity across the Permo-Triassic transition. This decrease in intensity is anomalous considering its coincidence with the climate warming at the Permo-Triassic transition, which tends to elevate chemical weathering rate of basalts and produce sediments with high chemical weathering intensity. Combining these weathering trends with present-day basalt weathering-temperature relationship and reported paleo-temperatures, total erosion rate is quantitatively estimated to increase from 282 ± 43 t/km^2/yr in the latest Permian to $> 1618 \pm 187$ t/km^2/yr in the Early Triassic. This massive erosion in the Early Triassic is plausibly related to amplified extreme precipitation associated with intensification of the hydrological cycle in the Early Triassic hothouse climate. This study underlines the weathering responses of tropical landscapes to rapid climate warming.

© 2021 Elsevier B.V. All rights reserved.

1. Introduction

Basalt weathering is sensitive to climatic conditions, especially temperature, and plays an important role in the global flux of CO_2 consumption by silicate weathering (e.g., Dessert et al., 2001, 2003; Li et al., 2016; Chen et al., 2020). Weathering of basalts in the tropical humid belt has been advocated to cause large scale climate change in Earth's deep past (e.g., Kent and Muttoni, 2013; Yang et al., 2018). However, tracking tropical basalt weathering and its linkage with climate change is challenging because of the generally low temporal resolution of geological records and the lack of reliable proxies for basalt weathering. A rapid climate warming

by more than $10\,°C$ occurred across the Permo-Triassic boundary (e.g., Joachimski et al., 2012; Chen et al., 2016; Schobben et al., 2014; Shen et al., 2019). This rapid temperature increase has been causally linked to the massive emission of greenhouse gases (e.g., CO_2) from the Siberian Traps (e.g., Burgess et al., 2017) and led to a long-term hyperthermal event through the Early Triassic (Kump, 2018; Sun et al., 2012). During the late Permian-Early Triassic, South China was situated in the humid tropical zone and contained a massive expanse of basaltic volcanic rocks within the Emeishan Large Igneous Province (LIP) (e.g., Xu et al., 2004; Torsvik et al., 2014). Erosion of the Emeishan LIP resulted in the dispersal of a large volume of volcanic detritus into the nearby Youjiang Basin during the late Permian to Early Triassic (e.g., He et al., 2007; Yang et al., 2015). Such sediment products could provide critical clues to track chemical weathering in their basaltic source landscapes (e.g.,

* Corresponding author.
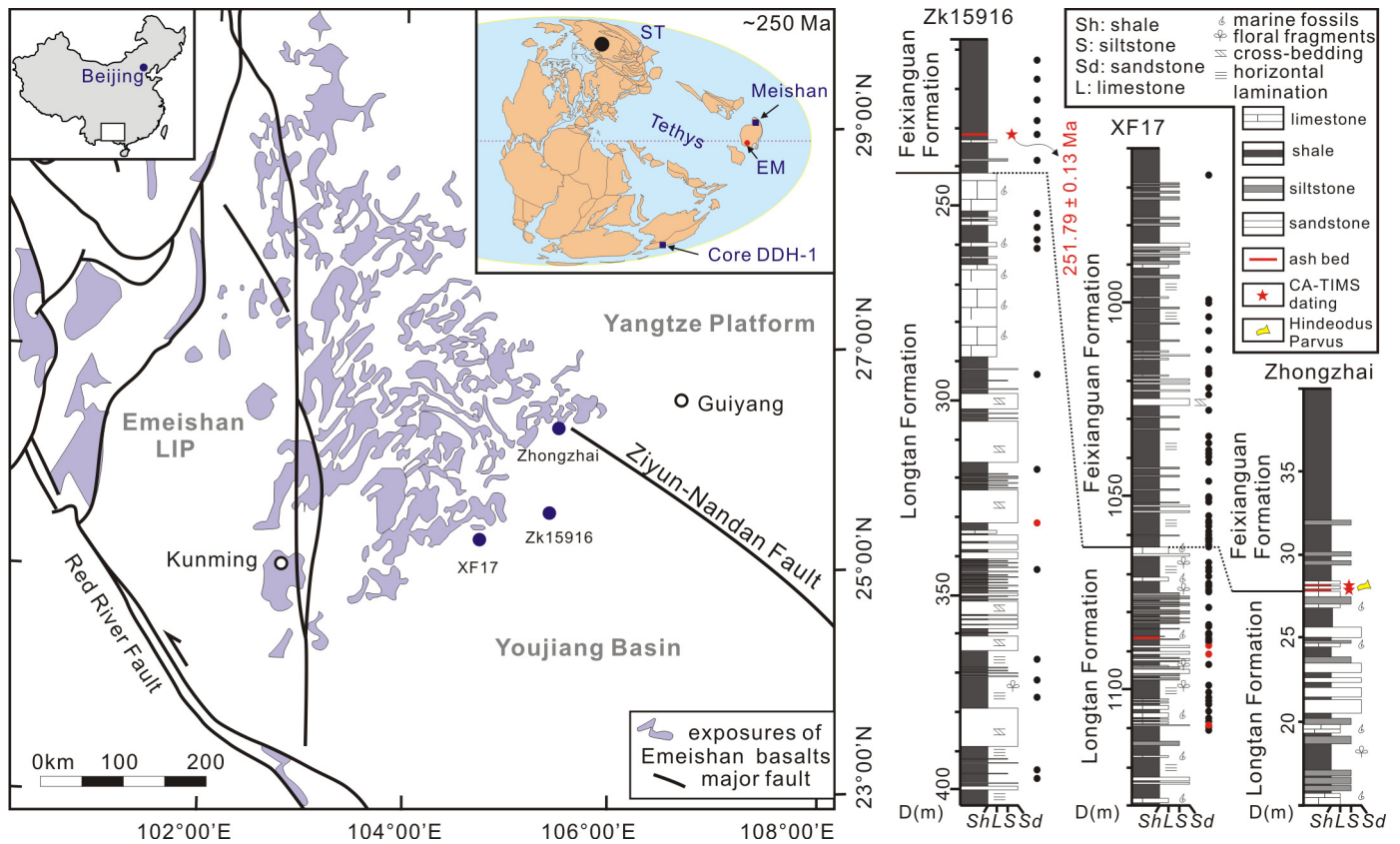*E-mail address:* yangjh@cug.edu.cn (J. Yang).

Fig. 1. Locations and stratigraphy of sampled successions in Zk15916 and XF17 core sections and compiled Zhongzhai Section (Shen et al., 2011). Also shown are the locations of Emeishan LIP (EM), Siberian Traps (ST), Meishan Section and core PHK Bunnerong DDH-1 (east Australia, Fielding et al., 2019) in the inset paleogeographic map of ~250 Ma (Torsvik et al., 2014). Dated claystone sample (red star) was collected at ~233 m from Core Zk15916. Obtained high-precision zircon U-Pb age and sampling locations for mudrocks (black dots) and sandstones (red dots) are presented with the columns. Studied core successions were correlated with the Zhongzhai Section, where the PTB has been well-constrained (Shen et al., 2011). (For interpretation of the colours in the figures, the reader is referred to the web version of this article.)

Sharma et al., 2013). We here focus on the Emeishan LIP derived sedimentary records in the northern Youjiang Basin and construct tropical basalt weathering trends across the Permo-Triassic transition. Results suggest an anomalous response of tropical basalt weathering to the Permo-Triassic warming and indicate massive erosion related to intensified hydrological cycle associated with the Early Triassic hothouse climate.

2. Geological settings and sampling successions

South China was situated in tropical latitudes during the Permian to Early Triassic with the Tethys Ocean to the west and the Panthalassa Ocean to the east (Fig. 1). Eastern South China includes the stratotype section for the Permian-Triassic boundary (Meishan Section, Fig. 1; e.g., Shen et al., 2011; Burgess et al., 2014). Western South China evolved as a passive margin until the Middle Triassic collisional orogeny between South China and the Simao-Indochina blocks (e.g., Wang et al., 2018). Late Permian massive magmatism in western South China formed the Emeishan LIP with an area of $\sim 3 \times 10^5$ km^2 in the eastern Tethyan coastal region (Fig. 1; Xu et al., 2004). This LIP was mainly emplaced around the Middle-Late Permian boundary (~259.5 Ma, Yang et al., 2018) with silicic volcanism extending to ~257.5 Ma (e.g., Zhong et al., 2020; Shell-nutt et al., 2020). Preserved volcanic sequences are dominated by flood basalts with minor amounts of pyroclastic and rhyolitic rocks. Basalts have been geochemically divided into high-Ti and low-Ti groups with the former stratigraphically overlying the latter in the western province and directly overlying Middle Permian carbonates in the eastern province (e.g., Xu et al., 2004; Xiao et al., 2004). Unconformably overlying the Emeishan LIP volcanic rocks are the

Late Permian-Early Triassic fluvial to deltaic siliciclastic rocks (e.g., Xu et al., 2004; He et al., 2007). These sedimentary rocks and their deep-water equivalents in the Youjiang Basin generally show an enrichment in volcanic fragments and feldspar grains for sandstones. Their chemical compositions are characterized by low SiO$_2$ contents and Al$_2$O$_3$/TiO$_2$ ratios, small or no negative Nb and Ta anomalies in the primitive mantle normalized trace element diagrams, and a small negative Eu anomaly in chondrite normalized rare earth element diagrams (e.g., He et al., 2007; Yang et al., 2015). They contain a small quantity of detrital zircons and yield a major zircon U-Pb age group at ~260 Ma (e.g., Yang et al., 2012, 2015; Deng et al., 2020). All these features suggest a dominant volcanic provenance from the Emeishan LIP. This provenance interpretation is consistent with a major south-flowing drainage system in the Emeishan LIP region in western South China during the Late Permian to Early Triassic periods as denoted by the paleogeographic reconstructions (Liu and Xu, 1994). In this sedimentary system the source rocks have been quantitatively estimated to be primarily (~75%) composed of high-Ti basalts with subordinate (~25%) silicic volcanic rocks based on sandstone modal compositions and bulk-rock geochemical modelling (Yang et al., 2015).

From the northern Youjiang Basin, the Zk15916 and XF17 drill cores through the Permo-Triassic sedimentary successions, along with a correlative exposed section at Zhongzhai (Shen et al., 2011), were carefully logged and sampled (Fig. 1). The sampled Permo-Triassic strata consist of the upper Longtan and lower Feixianguan formations that accumulated in an estuarine to shallow marine environment (Liu and Xu, 1994). The upper Longtan Formation contains dark grey mudrocks usually with horizontal lamination, fine-grained sandstone with interlaminated beds of mudrocks, cross-
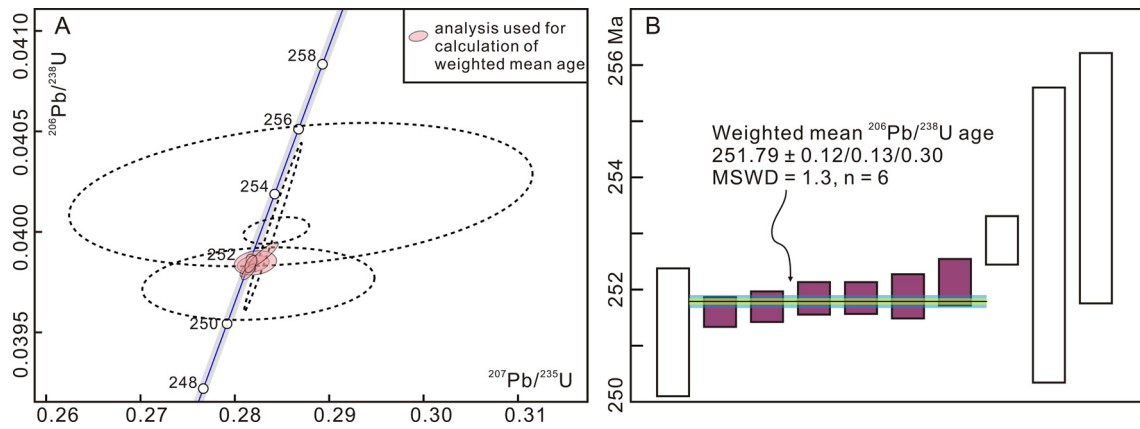
Fig. 2. CA-TIMS zircon U-Pb dating results for the claystone sample from Core Zk15916. (A) Zircon U-Pb concordia diagram for all analyses where those marked by dash cycles are not included the average age calculation. (B) Distribution of obtained $^{206}Pb/^{238}U$ dates and six of them were used to calculate a weighted mean age of 251.79 ± 0.12/0.13/0.36 Ma.

bedded sandstones, and limestones. The lower Feixianguan Formation contains reddish brown mudrocks, fine-grained sandstone with interlaminated mudrock, cross-bedded sandstones, and limestones (Fig. 1). Intercalated ash beds occur in the uppermost Longtan and lowest Feixianguan Formation. Sandstones are litharenites and rich in basaltic fragments with lathwork textures (Deng et al., 2020; Cawood, 1983).

3. Analytical methods

Mudrock and sandstone samples were collected from the upper Longtan Formation and lower Feixianguan formations in Zk15916 and XF17 core successions. Total organic carbon (TOC) content and organic carbon isotopes ($\delta^{13}C_{org}$, normalized to the international Vienna Peedee Belemnite (VPDB) standard) were analyzed in the State Key Laboratory of Environmental Geochemistry, Institute of Geochemistry Chinese Academy of Sciences. Analytical precisions for TOC and $\delta^{13}C_{org}$ are typically better than 0.2% and 0.03‰, respectively. Mineralogical analyses by X-ray diffraction were performed with a PANalytical X'Pert Pro model instrument at the State Key Laboratory of Geological Process and Mineral Resources (GPMR), China University of Geosciences (Wuhan). The analytical error is 5% for clay minerals (such as illite and chlorite, if illite content is 35%, it should be 35 ± 5%) and 2% for non-clay minerals (such as quartz and feldspar, if quartz content is 35%, it should be 35 ± 2%). Major elements were measured using a PANalytical Axios X-ray florescence spectrometer at ALS Chemex (Guangzhou, China). Analytical uncertainty is 5% for LOI (loss on ignition) and 2% for SiO_2, Al_2O_3, CaO, Fe_2O_{3T}, Na_2O, K_2O, MgO, MnO and P_2O_5. Determination limit is 0.01% for the major elements. Analysis of trace element concentrations was conducted on an Agilent 7500a ICP-MS (Inductively Coupled Plasma Mass Spectrometry) at the State Key Laboratory of Biogeology and Environmental Geology, CUG Wuhan. Analytical precision is generally better than 5% for most trace elements.

A tuff claystone (Zk15916-105) from Core Zk15916 was analyzed for high-precision zircon U-Pb dating by the CA-TIMS (chemical abrasion-thermal ionization mass spectrometry) method. Sample preparation and analyses were carried out at the NERC Isotope Geosciences Laboratory (NIGL), British Geological Survey (BGS), Nottingham, UK. Collected zircon grains were first thermally annealed and chemically abraded, and then spiked with ET2535 tracer solution (Condon et al., 2015) and totally dissolved. After anion-exchange chemistry, U and Pb were separated, and their isotope ratio measurements were made using a Thermo-Electron Triton Thermal Ionization Mass-Spectrometer in NIGL, BGS. Detailed

analytical methods and data are available in the Supplementary materials.

4. Results

4.1. High-precision CA-TIMS zircon U-Pb age

Sample Zk15916-105 was collected from a greenish grey claystone bed. Nine elongate zircon grains were selected for CA-TIMS analysis from this sample. They gave $^{206}Pb/^{238}U$ dates ranging from 251.2 Ma to 254.0 Ma and are characterized by a small variation in Th/U ratio of 0.52-0.76. This age distribution argues against reworking of older sediments because recycling of Emeishan LIP-derived sediments would provide ~260 Ma detrital zircons, which are not detected in the dated claystone sample. Six of the dated zircon grains yield a weighted mean $^{206}Pb/^{238}U$ date of 251.79 ± 0.12/0.13/0.36 Ma (date shown with analytical/analytical + tracer solution/analytical + tracer solution + decay constant uncertainties; Fig. 2; Table S1). This date is interpreted to mark the timing of volcanic eruption responsible for the claystone bed and thus represents the time of claystone deposition.

4.2. Bulk-rock organic carbon isotopes

A total of 49 mudrock and 2 fine-grained sandstone samples from Core XF17 and 15 mudrock and 2 fine-grained sandstone samples from Core Zk15916 were analyzed. They present a large variation in both TOC content (from 7.87% to 0.05% for most samples except two with extremely high TOC contents of 15.23% and 35.19%) and $\delta^{13}C_{org}$ value (from −23.19 ‰ to −29.5‰). There is no observable difference between fine-grained sandstone and mudrock samples in TOC content and $\delta^{13}C_{org}$ value. The two sampled successions display a consistent sequential pattern in TOC content and $\delta^{13}C_{org}$ ratio, with a large decrease across the boundary between the Longtan and Feixianguan formations (Fig. 3A).

4.3. Mineralogical compositions

Seventy-one mudrock and four fine-grained sandstone samples were analyzed from cores XF17 and Zk15916. Major mineral components are quartz (8–54%), feldspar (albite, 0–50%), and clay minerals (12–66%), which are mainly chlorite, mixed illite/smectite and illite (Table S3, Fig. 3B-F). Both quartz and clay minerals show a general decreasing trend in content through the uppermost Longtan Formation to the lower Feixianguan Formation (Fig. 3B-C). Chlorite shows a general increasing trend and mixed illite/smectite
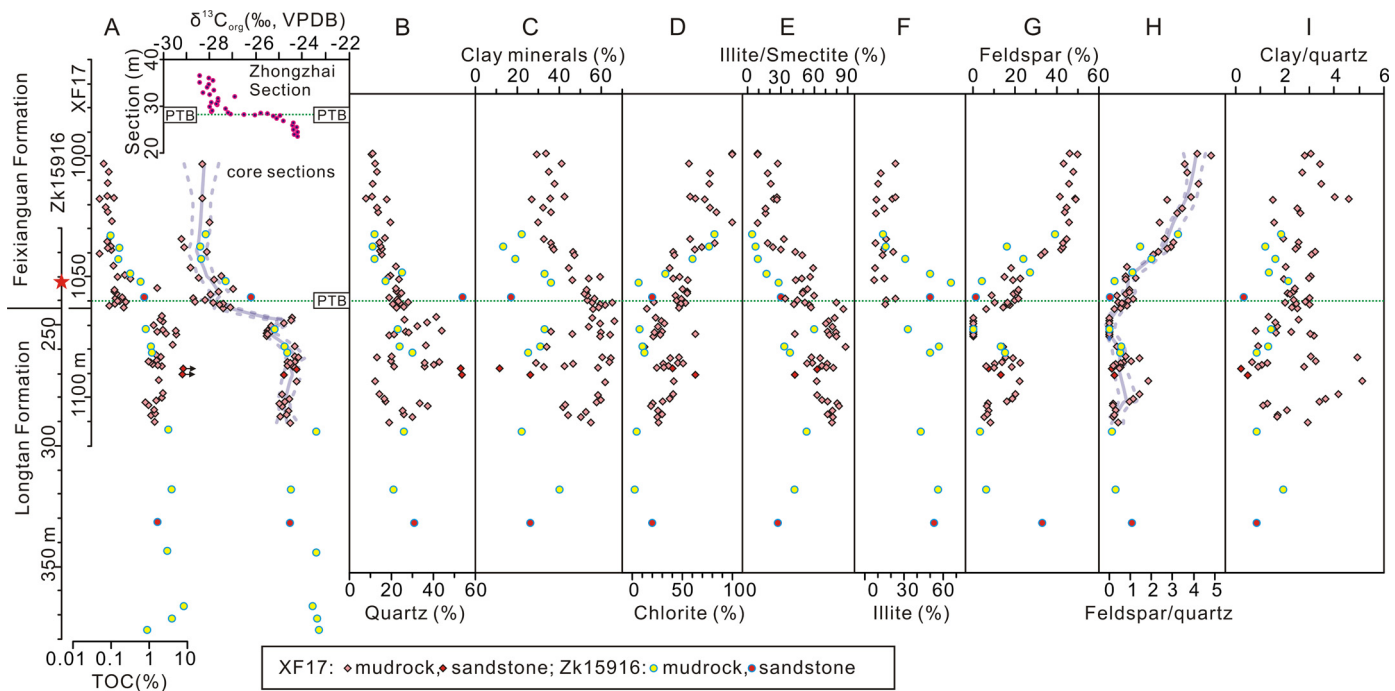
Fig. 3. Stratigraphic variations of TOC and $\delta^{13}C_{org}$ (A), contents of quartz (B) and clay minerals (C), relative contents of chlorite, mixed illite/smectite and illite in clay minerals (D, E and F), feldspar content (G), feldspar/quartz and clay/quartz ratios. Locally estimated scatterplot smoothing trendlines (0.2 smoothing, solid line) with 2.5% and 97.5% bootstrapped errors (dashed lines) are shown for $\delta^{13}C_{org}$ and feldspar/quartz ratio for core XF17 mudrock samples. Mudrocks of core Zk15916 plot on the smoothing trends of core XF17. The dashed green line marks the PTB, which was constrained by the new zircon U-Pb age and $\delta^{13}C_{org}$ correlations with the well-dated Zhongzhai Section (inset in A, Shen et al., 2011).

shows a generally decreasing trend through the uppermost Longtan Formation to the lower Feixianguan Formation. Illite is only detected in some samples of Feixianguan Formation (8–23%) for Core XF17 and shows a decrease in abundance from the upper Longtan (33–57%) to the lower Feixianguan (14–31%) Formation for Core Zk15916. Feldspar is nearly absent from the uppermost Longtan Formation and, along with feldspar/quartz ratio, displays a large increase through the lower Feixianguan Formation (Fig. 3G-H). Clay/quartz ratio exhibits a small variation (average value of 2.34) and is overall higher in mudrock samples than in sandstone samples (Fig. 3I). Non-silicate minerals are also detected, with calcite present in most samples, pyrite in some samples, and ankerite and siderite in a few samples (Table S3). Stratigraphically, pyrite is generally present in the dark grey mudrock samples of Longtan Formation but absent from the reddish brown mudrocks of Feixianguan Formation (Table S3). This variation is likely related to the redox conditions during deposition and diagenesis rather than source weathering because subaerial weathering cannot generate pyrite.

4.4. Major and trace element compositions

A total of 63 mudrock and 3 fine-grained sandstone samples from Core XF17 and of 15 mudrock and 2 fine-grained sandstone samples from Core Zk15916 were analyzed for major element compositions. They have variable concentrations of SiO_2 (24.5–54.5%), Al_2O_3 (5.1–19.5%), CaO (0.52–28.4%), K_2O (0.49–4.54%) and Na_2O (0.06–3.95%) and are generally rich in TiO_2 (most > 2.0%) (Table S4). In stratigraphy, Al_2O_3, SiO_2, CaO and TiO_2 do not show observable variations in contents, while Na_2O is higher in the lower Feixianguan Formation than in the uppermost Longtan Formation (Table S4; Fig. 4). There is a large variation in LOI (2.92-43.36), which is negatively correlated with CaO ($r^2 = 0.56$) for samples with low CaO (< 4%) and positively correlated with CaO ($r^2 = 0.64$) for samples with high CaO (> 4%) (Fig. S1). For both

the low and high CaO groups, LOI correlates negatively with SiO_2 ($r^2 = 0.75$ and 0.62, respectively). The low-CaO samples show a negative correlation and the high-CaO samples have no covarying relationship between LOI and TOC (Fig. S2). This suggests that the variation in LOI is largely related to carbonate contents for high-CaO samples and is mainly due to organic carbon content for low-CaO samples. Both TOC and carbonate increase could induce an increase in LOI content and result in low concentrations of Al_2O_3, TiO_2, SiO_2, K_2O and Na_2O, but TOC content is not accounted for in XRD analysis, and only the carbonate increase can lead to low contents of non-carbonate minerals like quartz, feldspar, and clay minerals (for Samples XF17-169 and XF17-172, their relatively low SiO_2 contents and high quartz concentrations could be possibly due to the correspondingly high TOC and low carbonate contents; recalculated SiO_2 contents without LOI are 62% and 55%, respectively; Tables S3 and S4). However, neither of the carbonate or TOC variation will cause changes to the elemental ratios like Al_2O_3/SiO_2 and Al_2O_3/TiO_2. The Al_2O_3/SiO_2 ratio varies in a small range (0.22–0.46 with an average of 0.31) for mudrock samples and is lower in sandstone samples (Fig. 4). The Al_2O_3/TiO_2 ratio displays a small variation for most samples (4.2–6.4 with an average of 5.1, Fig. 4) and is significantly lower than that of upper continental crust (30.4, Taylor and McLennan, 1985). These two ratios show no distinct variation through the sampled successions (Fig. 4).

Samples from Core Zk15916 were analyzed for trace element concentrations (Table S5). They have Y contents of 22.27–46.32 ppm, Th contents of 5.77–12.26 ppm, Sc contents of 11.26–29.32 ppm, Zr contents of 192.28–475.12 ppm and Nb contents of 25.40–65.51 ppm. Most samples have Th/Sc, Th/Nb, Nb/Y and La/Yb ratios in the range of 0.36–0.60, 0.18–0.26, 1.06–1.62 and 15.33–21.06, respectively. In contrast the two samples with higher Al_2O_3/TiO_2 ratios (7.61 and 11.22) have relatively higher Th/Sc (0.75 and 0.84) and Th/Nb ratio (0.38 and 0.46) and lower Nb/Y (0.77 and 0.88) and La/Yb (10.69 and 12.79) ratios.
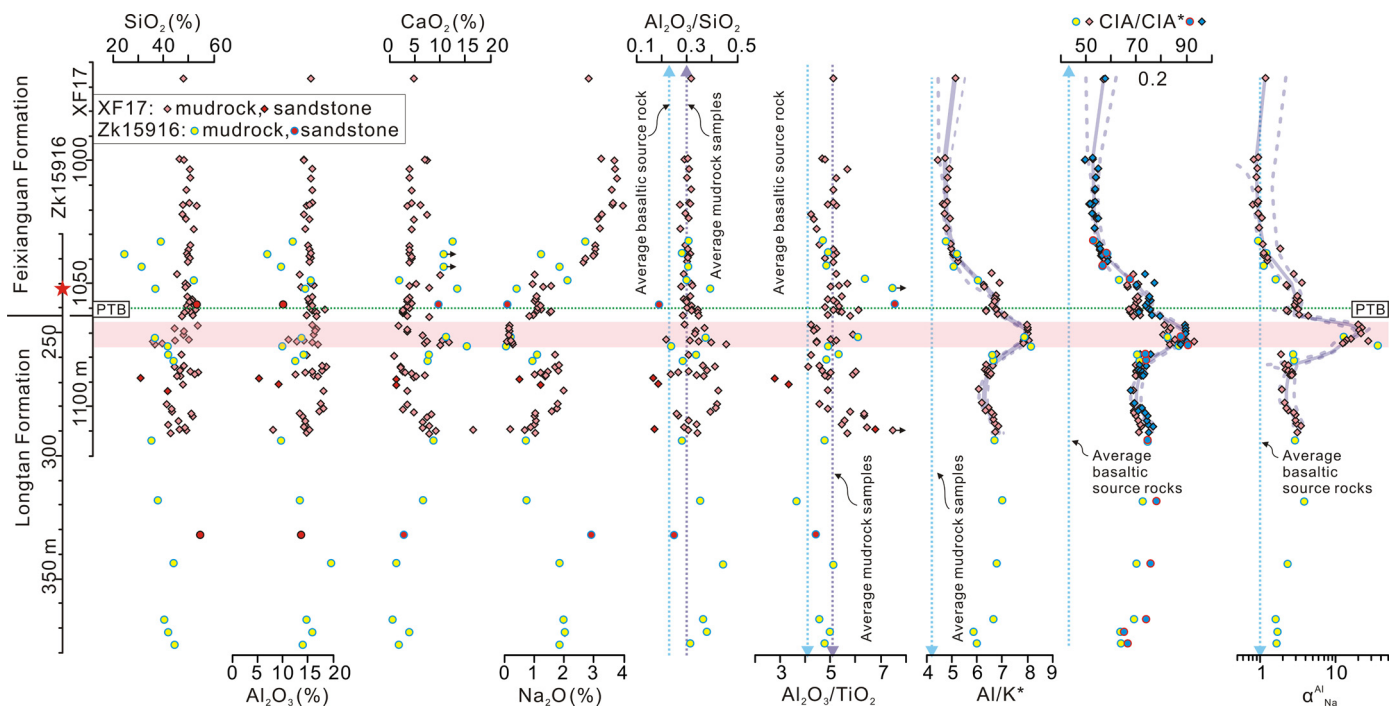
Fig. 4. Variations of SiO_2, Al_2O_3, CaO and Na_2O contents, Al_2O_3/SiO_2 and Al_2O_3/TiO_2 ratios and chemical weathering index values of Al/K^*, CIA, CIA^* and α^{Al}_{Na} through the sampled successions. Average values of Al_2O_3/SiO_2 and Al_2O_3/TiO_2 ratios for the mudrock samples are marked on the plots. Also indicated are the values of Al_2O_3/SiO_2, Al_2O_3/TiO_2, Al/K^*, CIA and α^{Al}_{Na} for the averaged basaltic source rocks (Yang et al., 2015). Locally estimated scatterplot smoothing trendlines (0.2 smoothing, solid line) with 2.5% and 97.5% bootstrapped errors (dashed lines) are shown for Al/K^*, CIA^* and α^{Al}_{Na} for core XF17 mudrock samples. Mudrocks of core Zk15916 plot on the smoothing trends of core XF17. The dashed green line marks the PTB and red star indicates the dated claystone bed. Pink shading indicates the interval with highest weathering intensity in the latest permian.

4.5. Chemical weathering index values

Major element compositions of mudrock samples were used to calculate weathering index values of WIP (weathering index of Parker, Parker, 1970), CIA (chemical index of alteration, Nesbitt and Young, 1982), α^{Al}_{Na} (Garzanti et al., 2013) and Al/K ratio (Bayon et al., 2012) to determine the source chemical weathering intensity and its temporal variations. For calculating WIP and CIA values, CaO in silicate fractions (CaO^*) was determined following the method of McLennan (1993). We use previously estimated average basaltic source rock composition for the Permo-Triassic sedimentary rocks of the Youjiang Basin (Yang et al., 2015) to calculate α^{Al}_{Na} values. Analyzed samples, along with the kinetically predicted weathering trend for basaltic source rock (Nesbitt and Young, 1984), were plotted on the A-CN-K (Al_2O_3–CaO+Na_2O–K_2O) diagram (Fig. 5A). Samples should plot on this trend, but some of the samples with higher CIA values (> 60) plot well below it and are inferred to have undergone diagenetic K metasomatism as suggested for sedimentary products or paleo-weathering profiles with source rocks of various igneous compositions including basaltic volcanic rocks (Nesbitt and Young, 1989; Fedo et al., 1995). Mudrocks are rich in clay minerals and their K metasomatism process is dominated by the conversion of clay minerals to illite, which along with mixed illite/smectite minerals are rich in studied samples with higher CIA values. For this type of K metasomatism, it follows a path toward the K_2O apex of the A-CN-K triangle plot. Both the amount of K enrichment and the paleo-weathering index prior to such enrichment can be ascertained from the A-CN-K diagram. A line from the K apex through metasomatized sample intersects the predicted weathering trend as a point, which represents its pre-metasomatized composition (Fig. 5B). A paleo-weathering index (CIA^*) corrected for K enrichment can then be determined by reading off the CIA value (Fig. 5B; Fedo et al., 1995). Following this interpretation of K metasomatism

in A-CN-K plot (Fig. 5B), Yang et al. (2018) proposed calculations (tabulated in the Fig. 5) to get the corrected K_2O^* and CIA^* values. Obtained K_2O^* was then used to calculate K-metasomatism corrected CIA^*, WIP^* and Al/K^* values (Table S6). Calculated weathering index values display large variations with CIA^* ranging from 50–91 and show a major decrease through the uppermost Longtan Formation to the lowest Feixianguan Formation after a moderate increase in the uppermost Longtan Formation (Fig. 4). The lowest CIA^*, WIP^* and Al/K^* values for the mudrocks of Feixianguan Formation are close to or overlap with that of the average basaltic source rock (Fig. 4).

5. The Permo-Triassic boundary for the studied successions

The obtained high-precision age of 251.79 ± 0.12 Ma is slightly younger than the updated age of 251.902 ± 0.024 Ma from Meishan Section (Burgess et al., 2014) for the Permo-Triassic boundary (PTB). This dated sample and its adjacent sandstone (Zk15916-104) is characterized by higher Al_2O_3/TiO_2 and lower Nb/Y ratios than other samples. Such features along with the lack of Emeishan LIP-derived ~260 Ma zircons argue against the reworking of detritus in the dated claystone sample from the underlying strata that display dominant provenance from the Emeishan LIP (e.g., He et al., 2007; Yang et al., 2015). This high-precision age thus constrains an earliest Triassic age for the studied claystone bed. It is interesting to note that this claystone bed was collected from the lowermost part of Feixianguan Formation in Core Zk15916 and stratigraphically above an interval within the strata with a $\delta^{13}C_{org}$ negative excursion of ~2‰ (Fig. 3A). A similar $\delta^{13}C_{org}$ negative excursion is also observed around the boundary between Longtan and Feixianguan formations from Core XF17. Based on the $\delta^{13}C_{org}$ stratigraphic trends and similarity in lithofacies, the two studied successions can be stratigraphically correlated through the Upper Permian Longtan Formation to the lower Triassic Feixianguan Formation (Fig. 3A).
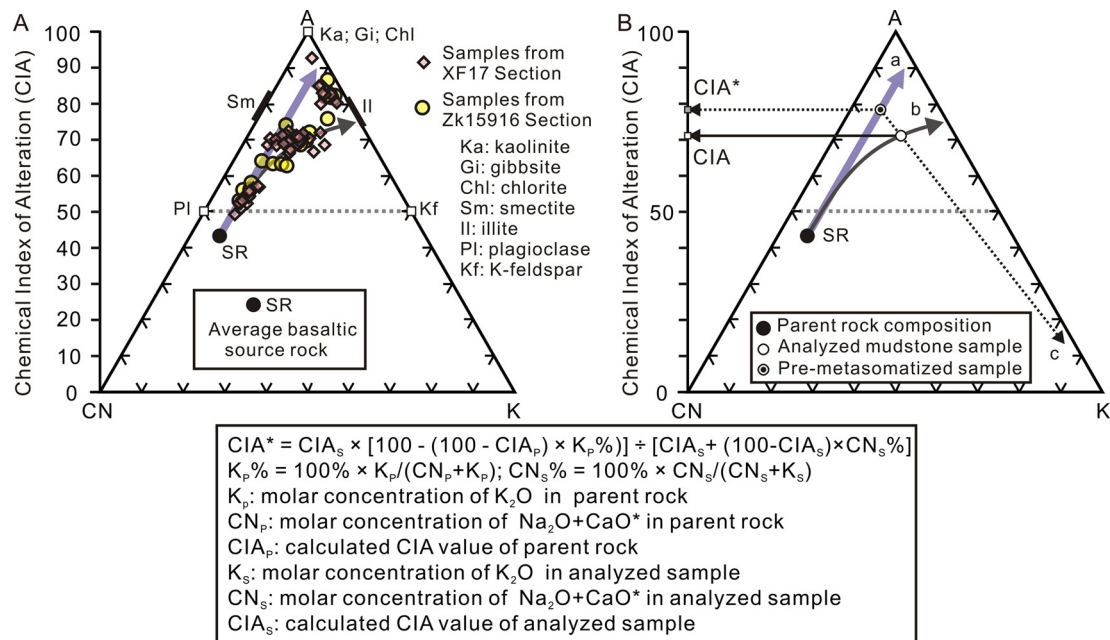
CIA* = CIA$_S$ × [100 - (100 - CIA$_P$) × K$_P$%)] ÷ [CIA$_S$+ (100-CIA$_S$)×CN$_S$%]
K$_P$% = 100% × K$_P$/(CN$_P$+K$_P$); CN$_S$% = 100% × CN$_S$/(CN$_S$+K$_S$)
K$_p$: molar concentration of K$_2$O in parent rock
CN$_P$: molar concentration of Na$_2$O+CaO* in parent rock
CIA$_P$: calculated CIA value of parent rock
K$_S$: molar concentration of K$_2$O in analyzed sample
CN$_S$: molar concentration of Na$_2$O+CaO* in analyzed sample
CIA$_S$: calculated CIA value of analyzed sample

Fig. 5. Plots of analyzed samples (A) and interpretations (B) on the A–CN–K (Al$_2$O$_3$–CaO*+Na$_2$O–K$_2$O) diagram with CIA values marked on the left. Also plotted on A are the average composition of basaltic source rocks (SR) as previously demonstrated (Yang et al., 2015), the predicted ideal weathering trend of SR and the general plotting trend of samples. Predicted weathering trend (arrow a) of SR, sample plotting trend (arrow b) and diagenetic addition of potassium to sediments (arrow c) are shown in B (Fedo et al., 1995). The CIA values of the plotted samples are lowered due to K-metasomatism effect. The pre-metasomatized CIA* value can be calculated on the interpretations of Fedo et al. (1995) using the compositions of average source rock according to the method outlined in Yang et al. (2018).

Though there is no high-precision age constraint for the succession in Core XF17, this stratigraphic correlation is supported by the demonstrated overlapping in stratigraphic variations of $\delta^{13}C_{Org}$ (Fig. 3A) and weathering index values (Al/K*, CIA* and α^{Al}_{Na}) between the two cores (Fig. 4).

Carbonate and organic carbon isotopic negative excursions have been documented at around the PTB (e.g., Shen et al., 2011). For typical marine successions, the PTB and associated carbon isotopic excursion is generally bio-stratigraphically constrained (e.g., Schobben et al., 2014; Joachimski et al., 2012). However, for non-marine successions, the organic carbon isotopic excursion is usually used to define the PTB and along with high-precision ages enables the level of the boundary to be constrained (e.g., Fielding et al., 2019). For the littoral successions in Zhongzhai section, the PTB has been well constrained based on high-precision zircon U-Pb dating and conodont biostratigraphy (Shen et al., 2011). A distinctive $\delta^{13}C_{Org}$ negative excursion is reported from the PTB interval at Zhongzhai (Fig. 3A; Shen et al., 2011). This well-dated Permo-Triassic succession could provide a critical reference to determine the PTB in the studied core successions, considering that the latter are geographically close to, and were deposited in, a sedimentary environment comparable to those in the Zhongzhai Section (Fig. 1; Liu and Xu, 1994). Based on the new zircon age and $\delta^{13}C_{Org}$ correlations to the Zhongzhai section, the PTB is tentatively constrained to levels of 240 m and 1060 m for the sampled Zk15916 and XF17 cores, respectively (Fig. 3). Although this placement of PTB needs to be confirmed by bio-stratigraphic studies in the future, our age constraint will not make a significant influence on the following discussion and conclusion.

6. Tropical basaltic weathering trends across the Permo-Triassic boundary

Most of the analyzed samples consistently have a small range and low Al$_2$O$_3$/TiO$_2$ ratios, in accord with a high-Ti basalt dominated provenance from the Emeishan LIP documented for the Late Permian to early Triassic sedimentary rocks in northern Youjiang

Basin (e.g., He et al., 2007; Yang et al., 2015, 2018). Detailed provenance analysis on the late Permian sedimentary rocks of Core XF17 confirmed their derivation from the basaltic rocks of the Emeishan LIP (Deng et al., 2020). The advocated high-Ti basalt dominated provenance is supported by the Nb/Y-Zr/TiO$_2$ diagram where all samples plot in the alkali-basalt field (Winchester and Floyd, 1977). They are partially overlapping with or close to the high-Ti basalts of the Emeishan LIP and are distinctly separated from the low-Ti basalts (Fig. 6A). This provenance interpretation is also supported by the chondrite and primitive mantle normalized spider diagrams where analyzed samples present similar geochemical characters as the high-Ti basalts, although there is a slight depletion in Eu and Ti and enrichment in Rb, Th and U for the samples relative to the high-Ti basalts (Fig. 6B-C). Therefore, the studied successions provide a potential record, in terms of variations in sediment compositions and calculated weathering index values, to track the chemical weathering trends of their tropical basaltic source (Nesbitt and Young, 1982; Bayon et al., 2012). However, change in source rock composition, sedimentary recycling, hydraulic sorting, and diagenesis can influence the compositions of terrigenous siliciclastic rocks and thus weathering index values (e.g., Fedo et al., 1995; Garzanti et al., 2013). These influences need to be properly evaluated prior to analysis of weathering trends.

An average source rock composition has been estimated as 75% high-Ti basalt and 25% silicic volcanic rocks from the Emeishan LIP for the Upper Permian sediments in the northern Youjiang Basin (Yang et al., 2015). Of this composite volcanic source rock, the silicic fraction would provide a likely source for the detrital quartz and zircon grains in these sediments (e.g., Yang et al., 2015; Deng et al., 2020). This average source rock of basaltic composition has a Al$_2$O$_3$/TiO$_2$ ratio of ca. 4.1 (Table S4) and was assumed for the analyzed successions. Compared to this average source rock, the two mudrock samples including the dated claystone have much higher Al$_2$O$_3$/TiO$_2$ ratios (11.2 for Zk15916-105 and 17.4 for XF17-156), consistent with a primary volcanic ash origin possibly related to the arc volcanisms in the Tethyan region (e.g., Yang et al., 2012). In contrast, all other mudrock samples have consis-
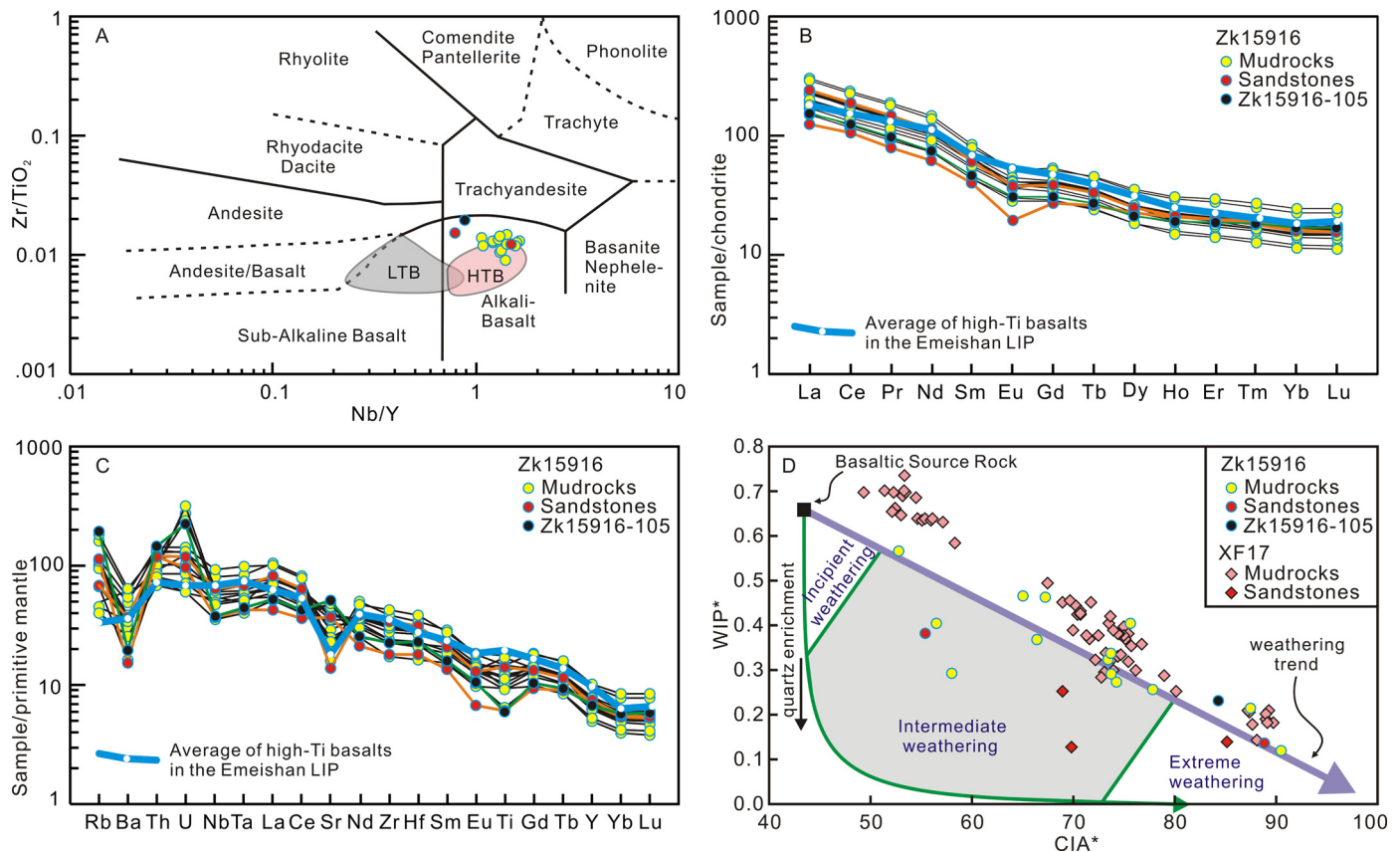
Fig. 6. Geochemical plots of Nb/Y vs. Zr/TiO₂ (A; Winchester and Floyd, 1977), chondrite (Sun and McDonough, 1989) normalized rare earth element pattern (B), primitive mantle (Sun and McDonough, 1989) normalized trace element spider (C) and CIA* vs. WIP* diagrams (D; Garzanti et al., 2013). CIA* vs. WIP* cross plot shows the weathering trend of the average basaltic source rock in the Emeishan LIP (Yang et al., 2015, 2018). Most samples plot along the source weathering trend and other four samples have WIP* values influenced by high contents of calcite, quartz, or pyrite. The geochemical data for the low-Ti basalts (LTB) and high-Ti basalts (HTB) of the Emeishan LIP are compiled from Xiao et al. (2004) and Xu et al. (2001).

tently low Al₂O₃/TiO₂ ratios, which are broadly comparable to that of this average source rock (Fig. 4). On the A-CN-K diagram (Fig. 5A; Fedo et al., 1995), the analyzed samples with low CIA values (< 60) plot on the predicted weathering trend of this advocated average source rock, supporting the assumption of average source rock composition. However, samples with higher CIA values generally plot below this source rock weathering trend (Fig. 5B). This can be interpreted as an indication of metasomatism induced K addition for both sedimentary rocks and paleo-weathering profiles derived from granitic or basaltic parent rocks (Nesbitt and Young, 1989; Fedo et al., 1995). Although the source of the extra potassium cannot be constrained based on the current data, correction for diagenetic K addition has been done according to A-CN-K plot (Fig. 5) and enables WIP*, CIA* and Al/K* values for mudrocks to be established (e.g., Fedo et al., 1995; Yang et al., 2018). It might be assumed that the event causing K metasomatism could also drive the mobility of Na. However, this assumption is seemly not possible because there is no correlation between K₂O and Na₂O contents ($r^2 = 0.01$) though more data are needed to verify the inactivity of Na during the K metasomatism process. The presence of authigenic pyrite and carbonate minerals also indicates diagenetic alterations, but this kind of diagenesis is unlikely to change the calculated weathering index values except that of WIP (e.g., Yang et al., 2018; Garzanti et al., 2013). Compared with sandstones, mudrocks have overall higher clay/quartz and Al₂O₃/SiO₂ ratios (Fig. 4) that are likely due to the hydraulic sorting induced enrichment of Al-bearing clay minerals in muddy sediments (e.g., Bouchez et al., 2012; Garzanti et al., 2013). But for mudrock samples themselves, they have a small variation (standard deviation is 0.05 and 0.99 for Al₂O₃/SiO₂ and clay/quartz ra-

tios, respectively) in these ratios through the sampled successions and dominantly plot along the basaltic source weathering trend in the WIP*-CIA* diagram (Fig. 6D). In addition, their weathering index values (e.g., CIA*) are poorly correlated with Al₂O₃/SiO₂ ratio ($r^2 = 0.03$). These characteristics suggest that hydraulic sorting and sedimentary recycling cannot explain the stratigraphic variations of mudrock compositions and thus the calculated weathering index values. The stratigraphic changes in values of CIA*, Al/K* and α^{Al}_{Na} of mudrock samples, excluding those with high Al₂O₃/TiO₂ ratios, thus are considered to reflect chemical weathering trends for their basaltic source in the Emeishan LIP.

These chemical index-based weathering trends denote a peak weathering intensity in the latest Permian followed by a distinct and progressive decrease through the Early Triassic (Fig. 4). They are consistent with the variations of mudrock mineralogical compositions, especially of the feldspar content and feldspar/quartz ratio (Fig. 3G-H). The absence of feldspars in the uppermost Permian mudrocks and the prominent increases in feldspar content and feldspar/quartz ratio through the end-Permian to earliest Triassic cannot be ascribed to hydraulic sorting effects because there are no corresponding changes in clay/quartz (Fig. 3) and Al₂O₃/SiO₂ ratios (e.g., Lupker et al., 2013; Fig. 4). A possible interpretation could be erosion of source rocks with more feldspars, but such source rocks would cause changes to the Al₂O₃/TiO₂ ratios of derived sediments, which are not observed from the sampled successions. Therefore, the lack of feldspars and the highest CIA*, Al/K* and α^{Al}_{Na} values from the uppermost Permian samples suggest extreme weathering of their basaltic source rocks resulting in few or no residual feldspars. In contrast, the high feldspar/quartz ratios and low CIA*, Al/K* and α^{Al}_{Na} values from the Early Trias-
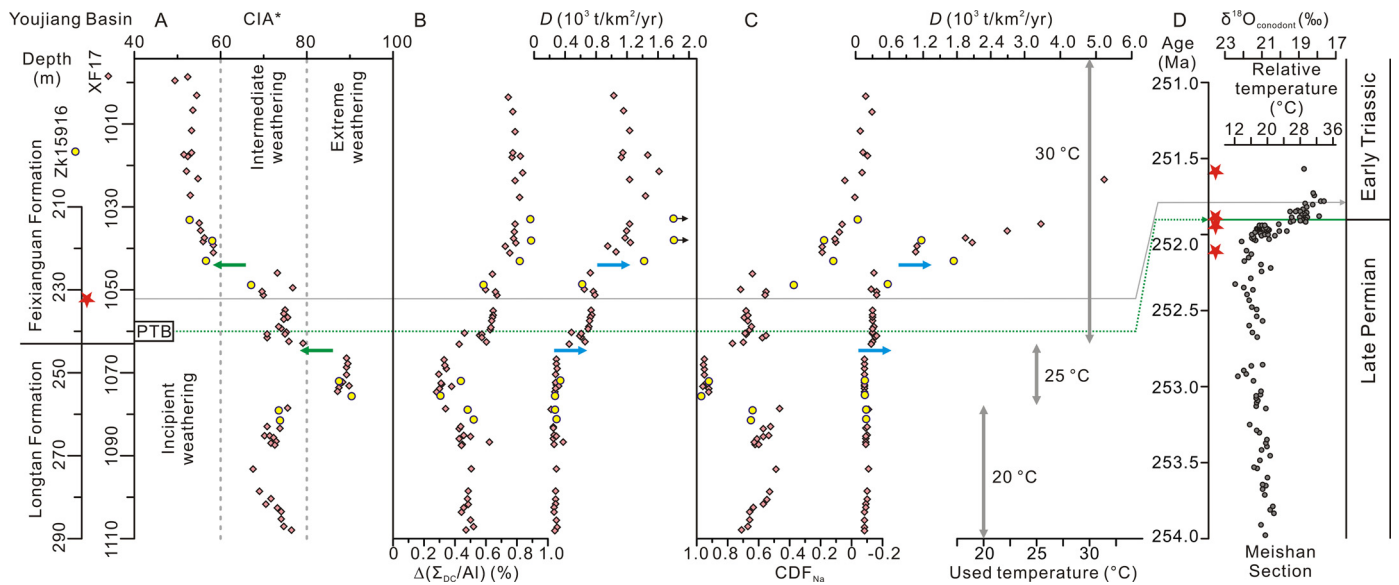
Fig. 7. Correlations of (A) CIA*, (B) $\Delta(\Sigma_{DC}/Al)$ and derived denudation rate (D), (C) CDF_{Na} and derived denudation rate (D) of the cored successions with (D) the conodont oxygen isotope ($\delta^{18}O_{conodont}$) variations from Meishan Section (Chen et al., 2016), the well-dated stratotype section for the Permo-Triassic transition (Burgess et al., 2014). Stratigraphical correlations between the cored successions and Meishan Section are based on the high-precision CA-TIMS zircon U-Pb ages (red stars; Burgess et al., 2014 for Meishan Section) around the Permo-Triassic boundary. Green dash line indicates the estimated PTB position and grey line indicates the high-precision age of 251.79 Ma reported in this study. Green arrows indicate decrease in weathering intensity and blue arrows indicate acceleration in total erosion for the tropical basaltic landscapes in South China through the Permo-Triassic transition.

sic mudrocks would reflect moderate-incipient weathering of the corresponding basaltic sources. These weathering trends are interpreted as indicating a significant transition from highly weathered basaltic landscapes to weakly weathered ones across the Permo-Triassic transition (from extreme weathering to incipient weathering; Fig. 7A).

7. Massive erosion of tropical basaltic landscapes in the Early Triassic

Based on the high-precision zircon U-Pb age and the negative carbon isotopic excursion, the constructed weathering trends show a significant decrease in basaltic weathering intensity temporally correlated with the rapid temperature increase, as indicated by the abrupt decrease of conodont $\delta^{18}O$ in the Meishan Section, at the Permo-Triassic boundary (e.g., Sun et al., 2012; Joachimski et al., 2012; Chen et al., 2016; Fig. 7). This decrease in basaltic weathering intensity is anomalous because chemical weathering tends to be critically accelerated in basaltic catchments of inactive volcanic fields with climate warming independent of variations in runoff (e.g., Li et al., 2016; Chen et al., 2020). Chemical weathering intensity can be expressed as the chemical depletion fraction (CDF) of sediments or regolith relative to their source rock or protolith (e.g., Riebe et al., 2004). It can be calculated based on the relative enrichment of an insoluble element i in the sediment (or regolith) relative to the source rock (or protolith), and linked with the chemical weathering rate (W) and denudation (total erosion) rate (D) in the source landscapes in steady-state weathering by

$$CDF = 1 - i_{source}/i_{sediment} = W/D = W/(W + E) \qquad (1)$$

where E is physical erosion rate, and $i_{sediment}$ and i_{source} represent concentrations of an insoluble element i (e.g., Zr, Ti and Al) in the sediment (or regolith) and source rock (or protolith), respectively (Riebe et al., 2004). Following this relationship, the Permo-Triassic decrease in weathering intensity would imply an acceleration in physical erosion. Rapid physical erosion is generally associated with short regolith residence time and results in

the incomplete weathering of eroded materials (e.g., West et al., 2005), like the tropical humid Puerto Rico fluvial sediments that have anomalously low weathering intensity related to mass wasting (Joo et al., 2018). We thus assume extremely high denudation rate for the studied sediments of the Lower Triassic Feixianguan Formation.

Modern rivers draining basaltic landscapes contain Ca, Mg, Na and K as the major cations and HCO_3^- as the major anion (e.g., Louvat and Allègre, 1997; Dessert et al., 2001, 2003; Chen et al., 2020), indicating bicarbonate dominant flux by chemical weathering of basalts. For inactive volcanic fields, there is a strong dependence of basaltic weathering rate and bicarbonate flux on mean annual temperature (Li et al., 2016). This correlation between weathering induced bicarbonate flux (f, 10^6 mol/km^2/yr) and temperature (T, °C) can be illustrated by

$$\ln(f) = 18.2(\pm 1.4) - 45.1(\pm 3.3) \times 1000/RT \qquad (2)$$

(Chen et al., 2020), where R is the universal gas constant (8.314 J/mol/K) and T is temperature in K. Though the exact land surface temperatures for the Emeishan LIP basaltic weathering through the late Permian to Early Triassic cannot be constrained, conodont $\delta^{18}O$ data for surface seawater paleotemperature have been reported from South China and suggest a temperature increase from $< 20\,°C$ to $> 35\,°C$ in this time period (e.g., Meishan Section, Fig. 7; Joachimski et al., 2012; Chen et al., 2016; Shen et al., 2019; Sun et al., 2012). Given the temperature range of $\sim-10\,°C$ to $\sim30\,°C$ used for the f-T transfer function (Chen et al., 2020) and the end-Permian rapid warming (e.g., Joachimski et al., 2012; Chen et al., 2016), we here assume that the temperature increased from $20 \pm 2\,°C$ for the late Permian pre-peak basaltic weathering, to $25 \pm 2\,°C$ for the latest Permian basaltic weathering peak, and then to $30 \pm 2\,°C$ for the post-peak basaltic weathering. Following Eq. (2) (Chen et al., 2020), the assumed temperatures would generate a basaltic weathering induced bicarbonate flux of $\sim0.74 \pm 0.11$ (10^6 mol/km^2/yr), $\sim1.01 \pm 0.13$ (10^6 mol/km^2/yr) and $\sim1.36 \pm 0.17$ (10^6 mol/km^2/yr), respectively. From these bicarbonate fluxes, the corresponding flux of individual cations can also be calculated. The obtained weathering induced Na fluxes (f_{Na}) are 0.13 ± 0.02

(10^6 mol/km^2/yr), 0.17 ± 0.02 (10^6 mol/km^2/yr) and 0.23 ± 0.03 (10^6 mol/km^2/yr), respectively, by using the proportion (17.2%) of Na in the total dissolvable cation (Σ_{DC}, Ca + Mg + Na + K) equivalent charge concentration ($\Sigma_{DCsource} = 5.3$ mol/kg, Table S7) for the average basaltic source rock and assuming a congruent dissolution of these elements in this basaltic source.

Taking the sediment compositions, the total erosion rate (D) can be calculated by

$$D = f / \Sigma_{DCsource} / [1 - \Delta(\Sigma_{DC}/Al)] \tag{3}$$

(Chen et al., 2020), where $\Delta(\Sigma_{DC}/Al)$ is the retention of Σ_{DC} based on Σ_{DC}/Al equivalent charge ratio of the sediments relative to the average basaltic source rock ($\Sigma_{DC}/Al = 0.70$ mol/mol, Table S7). Along with the values of Σ_{DC} (1.2–5.1 mol/kg), Σ_{DC}/Al (0.20–0.62 mol/mol) and $\Delta(\Sigma_{DC}/Al)$ (28–89%) for the analyzed mudrock samples (Table S6), the denudation rate was quantitatively estimated from 206 ± 32 t/km^2/yr to 2372 ± 312 t/km^2/yr (Table S7) and shows a significant increase from $\sim$290 t/km^2/yr in the latest Permian to $\sim$550 t/km^2/yr at around the PTB and then to > 2000 t/km^2/yr in the Early Triassic (Fig. 7A).

Denudation rate can also be estimated by rearranging Eq. (1) to

$$D = W / CDF = W / (1 - i_{source}/i_{sediment}) \tag{4}$$

(Riebe et al., 2004). It should be noted that the calculated CDF values might not reflect source weathering intensity of sedimentary rocks because of hydraulic sorting and diagenesis. For example, hydraulic sorting can result in higher concentrations of Zr and Ti in sands than in muds, and insoluble element concentrations of sedimentary rocks would be diluted by precipitation of diagenetic minerals. According to Riebe et al. (2004), Eq. (4) can also be written to express chemical weathering rates and chemical depletion fractions for an individual element (W_j and CDF$_j$):

$$D = W_j / (CDF_j \times j_{source})$$
$$= W_j / (j_{source} - j_{sediment} \times i_{source}/i_{sediment}) \tag{5}$$

where j_{source} and $j_{sediment}$ represent concentrations of a soluble element j in source rock and sediment, respectively. Considering the influences of hydraulic sorting on Zr and Ti, and of diagenesis on Ca, Mg and K, we here use Al as insoluble element i to calculate CDF$_{Na}$ and combining with the obtained f_{Na}, to calculate the denudation rate:

$$D = f_{Na} \times M_{Na} / (Na_{source} \times CDF_{Na}) \tag{6}$$

where M_{Na} is the molar mass of sodium (23 g/mol). CDF$_{Na}$ has a large variation from -0.25 to 0.97 for the mudrock samples used for weathering trend analysis (Table S7). Negative CDF$_{Na}$ values might indicate an underestimation of Na concentration for the average basaltic source rock. Excluding these negative CDF$_{Na}$ values, calculated D ranges from 188 ± 29 t/km^2/yr to 5406 ± 720 t/km^2/yr (Table S7) and also exhibit a great increase from $\sim$200 t/km^2/yr in the latest Permian to $\sim$400 t/km^2/yr at around the PTB and then to > 2500 t/km^2/yr in the earliest Triassic (Fig. 7B).

In comparison, estimated denudation rate from Eq. (3) is generally higher than that from Eq. (6) for $D < 1000$ t/km^2/yr and the former is much lower than the latter for $D > 1000$ t/km^2/yr. It should be noted that these estimates for denudation rate might have large errors considering the uncertainties associated with the inferred source rock composition and land surface temperature. Also the validity of the used basalt weathering-temperature relationship (Eq. (2)), proposed by Chen et al. (2020), needs to be considered. Eq. (2) was constructed based on chemical weathering data from basaltic fields that are inactive, which generally have low erosion rates (Li et al., 2016; Chen et al., 2020). So, the appli-

cability of Eq. (2) to regions with high denudation rates still has to be verified.

8. Intensified extreme precipitation in the Early Triassic hothouse

The constructed high-resolution erosional records for the tropical basaltic landscapes in the Emeishan LIP suggest two stages of denudation rate rapid increase separated by the new high-precision zircon U-Pb age (Fig. 7). The first one with an increase in denudation rate by $\sim$2 times occurred at the end-Permian and is associated with an extreme to intermediate weathering shift in the Emeishan basaltic landscapes (Fig. 7A). It is temporally correlated with end-Permian catastrophic soil erosion (e.g., Sephton et al., 2005; Retallack, 2005) and abrupt influx of terrigenous siliciclastics to carbonate platforms (e.g., Algeo and Twitchett, 2010). These erosional events were generally related to the end-Permian destruction of land vegetation (e.g., Sephton et al., 2005; Retallack, 2005; Algeo and Twitchett, 2010; but see Fielding et al., 2019 who argued for no exceptional erosional events at the end-Permian floristic turnover in the Sydney Basin). Our weathering trends for the basaltic landscapes in South China indicate sediments were generated from weathered soils and are consistent with massive soil erosion at the Permian-Triassic boundary (e.g., Algeo et al., 2011).

The second accelerating event is even more pronounced with an increase in denudation rate by $\sim$4–10 times in the Early Triassic. It is associated with a shift in the weathering intensity in the Emeishan basaltic landscape from intermediate to incipient (Fig. 7A) and an enhancement in bedrock erosion in the Early Triassic (Algeo et al., 2011). These Early Triassic high denudation rates (> 1500 t/km^2/yr) are much greater than that estimated for the modern basaltic landscapes in the Deccan Traps ($\sim$200 t/km^2/yr to $\sim$400 t/km^2/yr, Dessert et al., 2001; Chen et al., 2020) and are in the same order as that determined for the tropical basaltic landscapes in Réunion island ($\sim$1200 t/km^2/yr to $\sim$9300 t/km^2/yr, Louvat and Allègre, 1997). For the Réunion basaltic landscapes, the erosion rates are among the highest global estimates and were ascribed to high runoff, high relief, active volcanics and tectonics (Louvat and Allègre, 1997). For the Early Triassic basaltic landscapes in the Emeishan LIP, regional geological data indicate that there were no active tectonics along the passive margin of western South China (e.g., Wang et al., 2018) and the Emeishan LIP basaltic volcanism had terminated 7 Myrs earlier (e.g., He et al., 2007; Zhong et al., 2020; Yang et al., 2018). Sediment flux modelling suggested a paleorelief of ca. 200 m for the latest Permian landscapes in the Emeishan LIP (Wang et al., 2020) and implied a topography much flatter than that on the island of Réunion (> 2500 m high, Louvat and Allègre, 1997). Given the stable tectonic settings, we assume no significant change to the paleorelief for the Early Triassic landscapes of the Emeishan LIP. Therefore, the estimated Early Triassic high erosion rates cannot be related to high relief and steep slopes. Recent studies on Puerto Rico landscapes argued for a linkage of massive erosion with storm triggered frequent landslides (Joo et al., 2018) and proposed significant impacts of landslides on basin-scale erosion through extensive mass movement (Grande et al., 2021). In the basaltic island of Réunion, erosion rates are correlated with cyclone-driven variability of precipitation and are extraordinarily high where the difference in intensity between extreme rainfall events and prevailing precipitation is the strongest (Gayer et al., 2019). The Early Triassic is a period of hothouse climate with potential increase in tropical cyclone frequency and intensity (e.g., Kidder and Worsley, 2004; Schobben et al., 2014). Storm-generated depositional events have been widely reported from the Early Triassic successions in South China and other regions (e.g., Beatty et al., 2008; Kidder and Worsley, 2004; Pruss et

al., 2006). We thus envisage strong tropical cyclones in the Early Triassic hothouse, which intensify extreme precipitation for the western South China, and result in transient high runoff, and, along with the scarcity of terrestrial vegetation and continental aridification (e.g., Benton and Newell, 2014), could lead to the massive erosion of Emeishan basaltic province.

9. Conclusions

The Emeishan LIP derived sediments that accumulated in the adjoining Youjiang Basin have mineral and chemical compositions related to their basaltic source weathering in tropical latitudes during the latest Permian to Early Triassic. Weathering trends for these basaltic landscapes reflect an overall evolution from extreme to intermediate and then to incipient weathering through the latest Permian to Early Triassic. Combining the mudrock-indicated basaltic source weathering intensity with previously reported paleotemperatures and present-day temperature control on basalt weathering, we calculate the total erosion rates for the Emeishan basaltic landscapes through the late Permian to Early Triassic. Our estimates of erosion rate show two rapid accelerating events. Based on the new high-precision tuff zircon U-Pb age, the first event is constrained at the end-Permian and led to a $\sim$2 times increase in erosion rate and likely correlates with the massive soil erosion related to the end-Permian destruction of land vegetation. The second erosion accelerating event is much greater with an increase by more than $\sim$4 times and correlates with massive bedrock erosion in the Early Triassic. Calculated Early Triassic high erosion rates of > 1500 t/km^2/yr are similar to those determined for Réunion island and are among the highest global estimates calculated on the present day Earth. Such massive erosion is plausibly related to storm-induced extreme precipitation and transient high runoff during strong and frequent tropical cyclone events hypothesized for the Early Triassic hothouse climate.

CRediT authorship contribution statement

Jianghai Yang: Conceptualization, Funding acquisition, Investigation, Project administration, Resources, Writing – original draft. **Peter A. Cawood:** Funding acquisition, Writing – review & editing. **Dan J. Condon:** Investigation. **Jianzhong Liu:** Investigation, Resources. **Xusheng Deng:** Investigation, Resources. **Jingfu Wang:** Investigation. **Yuansheng Du:** Investigation. **Dongxun Yuan:** Investigation.

Declaration of competing interest

The authors declare that they have no known competing financial interests or personal relationships that could have appeared to influence the work reported in this paper.

Acknowledgements

Appendix A. Supplementary material

Supplementary material related to this article can be found online at https://doi.org/10.1016/j.epsl.2021.117256.

References

Algeo, T.J., Twitchett, R.J., 2010. Anomalous Early Triassic sediment fluxes due to elevated weathering rates and their biological consequences. Geology 38, 1023–1026.

Algeo, T.J., Chen, Z.Q., Fraiser, M.L., Twitchett, R.J., 2011. Terrestrial-marine teleconnections in the collapse and rebuilding of Early Triassic marine ecosystems. Palaeogeogr. Palaeoclimatol. Palaeoecol. 308, 1–11.

Bayon, G., Dennielou, B., Etoubleau, J., Ponzevera, E., Toucanne, S., Bermell, S., 2012. Intensifying weathering and land use in Iron Age Central Africa. Science 335, 1219–1222.

Beatty, T.W., Zonneveld, J.P., Henderson, C.M., 2008. Anomalously diverse Early Triassic ichnofossil assemblages in northwest Pangea: a case for a shallow-marine habitable zone. Geology 36, 771–774.

Benton, M.J., Newell, A.J., 2014. Impacts of global warming on Permo-Triassic terrestrial ecosystems. Gondwana Res. 25, 1308–1337.

Bouchez, J., Gaillardet, J., Lupker, M., Louvat, P., France-Lanord, C., Maurice, L., Armijos, E., Moquet, J.-S., 2012. Floodplains of large rivers: weathering reactors or simple silos? Chem. Geol. 332–333, 166–184.

Burgess, S.D., Bowring, S., Shen, S., 2014. High-precision timeline for Earth's most severe extinction. Proc. Natl. Acad. Sci. USA 111, 3316–3321.

Burgess, S.D., Muirhead, J.D., Bowring, S.A., 2017. Initial pulse of Siberian Traps sills as the trigger of the end-Permian mass extinction. Nat. Commun. 8, 164.

Cawood, P., 1983. Modal composition and detrital clinopyroxene geochemistry of lithic sandstones from the New England Fold Belt (east Australia): a Paleozoic forearc terrane. Geol. Soc. Am. Bull. 94, 1199–1214.

Chen, J., Shen, S.Z., Li, X.H., Xu, Y.G., Joachimski, M.M., Bowring, S.A., Erwin, D.H., Yuan, D.X., Chen, B., Zhang, H., Wang, Y., Cao, C.Q., Zheng, Q.F., Mu, L., 2016. High-resolution SIMS oxygen isotope analysis on conodont apatite from South China and implications for the end-Permian mass extinction. Palaeogeogr. Palaeoclimatol. Palaeoecol. 448, 26–38.

Chen, Y., Hedding, D.W., Li, X., Greyling, A.C., Li, G., 2020. Weathering dynamics of Large Igneous Provinces (LIPs): a case study from the Lesotho Highlands. Earth Planet. Sci. Lett. 443, 59–69.

Condon, D.J., Schoene, B., McLean, N.M., Bowring, S.A., Parrish, R.R., 2015. Metrology and traceability of U-Pb isotope dilution geochronology (EARTHTIME Tracer Calibration Part I). Geochim. Cosmochim. Acta 164, 464–480.

Deng, X., Yang, J., Cawood, P.A., Wang, X.-C., Du, Y., Huang, Y., Lu, S., He, B., 2020. Detrital record of late-stage silicic volcanism in the Emeishan large igneous province. Gondwana Res. 79, 197–208.

Dessert, C., Dupré, B., Gaillardet, J., François, L.M., Schott, J., Gaillardet, J., Chakrapani, G., Bajpai, S., 2001. Erosion of Deccan Traps determined by river geochemistry: impact on the global climate and the ^{87}Sr/^{86}Sr ratio of seawater. Earth Planet. Sci. Lett. 188, 459–474.

Dessert, C., Dupré, B., Gaillardet, J., François, L.M., Allègre, C.J., 2003. Basalt weathering laws and the impact of basalt weathering on the global carbon cycle. Chem. Geol. 202, 257–273.

Fedo, C.M., Nesbitt, H.W., Young, G.M., 1995. Unravelling the effects of potassium metasomatism in sedimentary rocks and paleosols, with implications for paleoweathering conditions and provenance. Geology 23, 921–924.

Fielding, C.R., Frank, T.D., McLoughlin, S., Vajda, V., Mays, C., Tevyaw, A.P., Winguth, A., Winguth, C., Nicoll, R.S., Bocking, M., Crowley, J.L., 2019. Age and pattern of the southern high-latitude continental end-Permian extinction constrained by multiproxy analysis. Nat. Commun. 10, 385.

Garzanti, E., Padoan, M., Setti, M., Najman, Y., Peruta, L., Villa, I.M., 2013. Weathering geochemistry and Sr-Nd fingerprints of equatorial upper Nile and Congo muds. Geochem. Geophys. Geosyst. 14, 292–316.

Gayer, E., Michon, L., Louvat, P., Garllardet, J., 2019. Storm-induced precipitation. Earth Planet. Sci. Lett. 517, 61–70.

Grande, A., Schmidt, A.H., Bierman, P.R., Corbett, L.B., Lopez-Lloreda, C., Willenbring, J., McDowell, W.H., Caffee, M.W., 2021. Landslides, hurricanes, and sediment sourcing impact basin-scale erosion estimates in Luquillo, Puerto Rico. Earth Planet. Sci. Lett. 517, 61–70.

He, B., Xu, Y.-G., Huang, X.-L., Luo, Z.-Y., Shi, Y.-R., Yang, Q.-J., Yu, S.-Y., 2007. Age and duration of the Emeishan flood volcanism, SW China: geochemistry and SHRIMP zircon U-Pb dating silicic ignimbrites, post-volcanic Xuanwei Formation and clay tuff at the Chaotian section. Earth Planet. Sci. Lett. 255, 306–323.

Joachimski, M.M., Lai, X., Shen, S., Jiang, H., Luo, G., Chen, B., Chen, J., Sun, Y., 2012. Climate warming in the latest Permian and the Permian-Triassic mass extinction. Geology 40, 195–198.

Joo, Y.J., Madden, M.E.E., Soreghan, G.S., 2018. Anomalously low chemical weathering in fluvial sediment of a tropical watershed (Puerto Rico). Geology 46, 691–694.

Kent, D.V., Muttoni, G., 2013. Modulation of Late Cretaceous and Cenozoic climate by variable drawdown of atmospheric pCO$_2$ from weathering of basaltic provinces on continents drifting through the equatorial humid belt. Clim. Past 9, 525–546.

Kidder, D.L., Worsley, T.R., 2004. Causes and consequences of extreme Permo-Triassic warming to globally equable climate and relation to the Permo-Triassic extinction and recovery. Palaeogeogr. Palaeoclimatol. Palaeoecol. 203, 207–237.

Kump, L.R., 2018. Prolonged Late Permian–Early Triassic hyperthermal: failure of climate regulation? Philos. Trans. R. Soc. A 376, 20170078.

Li, G., Hartmann, J., Derry, L.A., West, A.J., You, C.F., Long, X., Zhan, T., Li, L., Li, G., Qiu, W., Li, T., Liu, L., Chen, Y., Ji, J., Zhao, L., Chen, J., 2016. Temperature dependence of basalt weathering. Earth Planet. Sci. Lett. 443, 59–69.

Liu, B., Xu, X., 1994. Atlas of Lithofacies and Palaeogeography of South China (Sinian to Triassic). Science Press, Beijing, pp. 1–88 (in Chinese with English abstract).

Louvat, P., Allègre, C.J., 1997. Present denudation rates on the island of determined by river geochemistry: basalt weathering and mass budget between chemical and mechanical erosions. Geochim. Cosmochim. Acta 61, 3645–3669.

Lupker, M., France-Lanord, C., Galy, V., Lavé, J., 2013. Increasing chemical weathering in the Himalayan system since the Last Glacial Maximum. Earth Planet. Sci. Lett. 365, 243–252.

McLennan, S.M., 1993. Weathering and global denudation. J. Geol. 101, 295–303.

Nesbitt, H.W., Young, G.M., 1982. Early Proterozoic climates and plate motions inferred from major element chemistry of lutites. Nature 299, 715–717.

Nesbitt, H.W., Young, G.M., 1984. Prediction of some weathering trends of plutonic and volcanic rocks based on thermodynamic and kinetic considerations. Geochim. Cosmochim. Acta 48, 1523–1534.

Nesbitt, H.W., Young, G.M., 1989. Formation and diagenesis of weathering profiles. J. Geol. 97 (2), 129–147.

Parker, A., 1970. An index of weathering for silicate rocks. Geol. Mag. 107, 501–504.

Pruss, S.B., Bottjer, D.J., Corsetti, F.A., Baud, A., 2006. A global marine sedimentary response to the end-Permian mass extinction: examples from southern Turkey and the western United States. Earth-Sci. Rev. 78, 193–206.

Retallack, G.J., 2005. Earliest Triassic claystone breccias and soil-erosion crisis. J. Sediment. Res. 75, 679–695.

Riebe, C.S., Kirchner, J.W., Finkel, R.C., 2004. Erosional and climate effects on long-term chemical weathering rates in granitic landscapes spanning diverse climate regimes. Earth Planet. Sci. Lett. 224, 547–562.

Schobben, M., Joachimski, M.M., Korn, D., Leda, L., Korte, C., 2014. Palaeotethys seawater temperature rise and an intensified hydrological cycle following the end-Permian mass extinction. Gondwana Res. 26, 675–683.

Sephton, M.A., Looy, C.V., Brinkhuis, H.B., Wignall, P.B., de Leeuw, J.W., Visscher, H., 2005. Catastrophic soil erosion during the end-Permian biotic crisis. Geology 33, 941–944.

Sharma, A., Sensarma, S., Kumar, K., Khanna, P.P., Saini, N.K., 2013. Mineralogy and geochemistry of the Mahi River sediments in tectonically active western India: implications for Deccan large igneous province source, weathering and mobility of elements in a semi-arid climate. Geochim. Cosmochim. Acta 104, 63–83.

Shellnutt, J.G., Pham, T.T., Denyszyn, S.W., Yeh, M.-W., Tran, T.-A., 2020. Magmatic duration of the Emeishan large igneous province: insight from northern Vietnam. Geology 48, 457–461.

Shen, S.Z., Crowley, J.L., Wang, Y., Bowring, S.A., Erwin, D.H., Sadler, P.M., Cao, C.Q., Rothman, D.H., Henderson, C.M., Ramezani, J., Zhang, H., Shen, Y., Wang, X.D., Wang, W., Mu, L., Li, W.Z., Tang, Y.G., Liu, X.L., Liu, L.J., Zeng, Y., Jiang, Y.F., Jin, Y.G., 2011. Calibrating the end-Permian mass extinction. Science 334, 1367–1372.

Shen, S.Z., Ramezani, J., Chen, J., Cao, C.-Q., Erwin, D.H., Zhang, H., Xiang, L., Schoepfer, S.D., Henderson, C.M., Zheng, Q.-F., Bowring, S.A., Wang, Y., Li, X., Wang, X., Yuan, D., Zhang, Y., Mu, L., Wang, J., Wu, Y., 2019. A sudden end-Permian mass extinction in South China. Geol. Soc. Am. Bull. 131, 205–223.

Sun, S.S., McDonough, W.F., 1989. Chemical and isotopic systematics of oceanic basalts: implications for mantle composition and processes. Geol. Soc. (Lond.) Spec. Publ. 42, 313–345.

Sun, Y., Joachimski, M.M., Wignall, P.B., Chen, Y., Jiang, H., Wang, L., Lai, X., 2012. Lethally hot temperatures during the early Triassic greenhouse. Science 338, 366–370.

Taylor, S.R., McLennan, S.M., 1985. The Continental Crust: Its Composition and Evolution.

Torsvik, T.H., van der Voo, R., Doubrovine, P.V., Burke, K., Steinberger, B., Ashwal, L.D., Trønnes, R.G., Webb, S.J., Bull, A.L., 2014. Deep mantle structure as a reference frame for movements in and on the Earth. Proc. Natl. Acad. Sci. USA 111, 8735–8740.

Wang, Y., Qian, X., Cawood, P.A., Liu, H., Feng, Q., Zhao, G., Zhang, Y., He, H., Zhang, P., 2018. Closure of the East Paleotethyan Ocean and amalgamation of the Eastern Cimmerian and Southeast Asia continental fragments. Earth-Sci. Rev. 186, 195–230.

Wang, X., Shao, L., Eriksson, K.A., Yan, Z., Wang, J., Li, H., Zhou, R., Lu, J., 2020. Evolution of a plume-influenced source-to-sink system: an example from the coupled central Emeishan large igneous province and adjacent western Yangtze crationic basin in the Late Permian, SW China. Earth-Sci. Rev. 186, 195–230.

West, A.J., Galy, A., Bickle, M., 2005. Tectonic and climatic controls on silicate weathering. Earth Planet. Sci. Lett. 235, 211–228.

Winchester, J.A., Floyd, P.A., 1977. Geochemical discrimination of different magma series and their differentiation products using immobile elements. Chem. Geol. 20, 325–343.

Xiao, L., Xu, Y.G., Mei, H.J., Zheng, Y.F., He, B., Pirajno, F., 2004. Distinct mantle sources of low-Ti and high-Ti basalts from the western Emeishan large igneous province, SW China: implications for plume-lithosphere interaction. Earth Planet. Sci. Lett. 228, 525–546.

Xu, Y.-G., Chung, S.-L., Jahn, B.-M., Wu, G., 2001. Petrologic and geochemical constraints on the petrogenesis of Permian-Triassic Emeishan flood basalts in southwestern China. Lithos 58, 145–168.

Xu, Y.-G., He, B., Chung, S.-L., Menzies, M.A., Frey, F.A., 2004. Geologic, geochemical, and geophysical consequences of plume involvement in the Emeishan floodbasalt province. Geology 32, 917–920.

Yang, J., Cawood, P.A., Du, Y., Huang, H., Huang, H.W., Tao, P., 2012. Large igneous province and magmatic arc sourced Permian-Triassic volcanogenic sediments in China. Sediment. Geol. 261–262, 120–131.

Yang, J., Cawood, P.A., Du, Y., 2015. Voluminous silicic eruptions during late Permian Emeishan igneous province and link to climate cooling. Earth Planet. Sci. Lett. 432, 166–175.

Yang, J., Cawood, P.A., Du, Y., Condon, D.J., Yan, J., Liu, J., Huang, Y., Yuan, D., 2018. Early Wuchiapingian cooling linked to Emeishan basaltic weathering? Earth Planet. Sci. Lett. 492, 102–111.

Zhong, Y., Mundil, R., Chen, J., Yuan, D., Denyszyn, S.W., Jost, A.B., Payne, J.L., He, B., Shen, S., Xu, Y., 2020. Geochemical, biostratigraphic, and high-resolution geochronological constraints on the warming stage of Emeishan Large Igneous Province. Geol. Soc. Am. Bull. 132, 1969–1986.